Supplementary materials for:

Descriptor for the design of 2D MXenes hydrogen evolution reaction electrocatalysts

Changxing Wang[a,b,&], XiaoXu Wang[c,d,&], TianYao Zhang[e], Ping Qian[a,f,*], Turab Lookman[g,*], YanJin Su[a,b,*]

The appendix materials file includes:

Supplementary Text:

Ti_2CO_2-STM electrical conductivity and thermodynamic stability.

Supplementary Tables and Figures:

Table S1. Ti_2CO_2 free energy of three O atom site.

Table S2. ΔG_H of 1, 1/4, 1/9 and 1/16 H coverage for Ti_2CO_2.

Table S3. DFT-D3, optB86 and PBE results for Ti_2CO_2-STM.

Table S4. 3 Samples for the calculation of ΔE_{ZPE} - $T\Delta S_H$.

Table S5. Δh values between STM and Ti atoms layer in z axis.

Table S6. The comparation of ΔG_H and ΔG_H (H_2O).

Table S7. Descriptor subsets for GPR and SVR model.

Figure S1. Band structure of Ti_2CO_2 and Ti_2CO_2-V, Mn, Nb, Mo, W and Re.

Figure S2. Thermodynamic stability.

Figure S3. The correlation coefficients between Fermi level (E_f), P_z-band center of O (ε_{Opz}) and adsorption energy ΔG_H of S_0, S_1, S_2 sites.

Figure S4. Comparison of methods to simplify ΔEZPE - TΔSH.

Figure S5. ΔG_H^{pH} vs pH.

Figure S6. Deformation charge density and Bader analysis.

Figure S7. Effect of H_2O solvent.

Table S1. Ti_2CO_2 free energy of three O atom site.

Site	Free Energy (eV)
top	-41.267
fcc	-46.332
hcp	-44.529

Table S2. ΔG_H of 1, 1/4, 1/9 and 1/16 H coverage for Ti_2CO_2 (DFT-D3).

	$E_{Ti_2CO_2}$	$E_{Ti_2CO_2-H}$	E_H	ZEP	ΔG_H
1x1	-46.205	-49.312	-3.3867	0.3	0.579
2x2	-184.822	-188.313	-3.3867	0.3	0.195
3x3	-415.850	-419.428	-3.3867	0.3	0.109
4x4	-739.289	-742.855	-3.3867	0.3	0.120

Table S3. DFT-D3, optB86 and PBE results for Ti_2CO_2-STM.

Ti_2CO_2-STM Name	ΔG_H-S_0	ΔG_H-S_1	ΔG_H-S_2
Ag-DFT-D3	-0.85609935	-0.4608638	-0.47461648
Au-DFT-D3	-0.74686509	-0.21375962	-0.15312428
Cd-DFT-D3	-1.00974241	-0.62648962	-0.71560585
Co-DFT-D3	-0.65639116	-0.45996473	-0.41776365
Cr-DFT-D3	-0.40118437	-0.24384245	-0.23580838
Cu-DFT-D3	-0.83375736	-0.39191251	-0.50522517
Fe-DFT-D3	-0.3749933	-0.18110057	-0.13006822
Hf-DFT-D3	0.24053049	0.10605112	0.10175489
Ir-DFT-D3	-0.56875761	-0.4563445	-0.39167908
Mn-DFT-D3	-0.09787272	0.06921355	0.10628425
Mo-DFT-D3	-0.12551281	-0.03494635	0.03566989
Nb-DFT-D3	0.07412593	0.03896	0.06695144
Ni-DFT-D3	-0.34747101	-0.08830282	-0.07776402
Os-DFT-D3	-0.3813331	-0.27753513	-0.19652168
Pd-DFT-D3	-0.12956499	0.14112112	0.099247
Pt-DFT-D3	0.03984849	0.12602008	0.20184017
Re-DFT-D3	-0.1312155	-0.04230939	0.01529681
Rh-DFT-D3	-0.64333312	-0.50381069	-0.45946523
Ru-DFT-D3	-0.48416922	-0.35237507	-0.29065927
Sc-DFT-D3	-0.48717301	-0.41797811	-0.45723971

Ta-DFT-D3	0.17030543	0.04075588	0.08450423
Ti-DFT-D3	0.10887018	0.10887059	0.10887144
V-DFT-D3	-0.12643408	0.01727684	0.05935475
W-DFT-D3	-0.02282339	2.988E-05	0.07327152
Y-DFT-D3	-0.55703464	-0.42770457	-0.48510709
Zn-DFT-D3	-0.98170029	-0.62031463	-0.67713902
Zr-DFT-D3	0.23463941	0.10697383	0.09660171
Ag-optB86	-0.67659	-0.29131	-0.30241
Au-optB86	-0.56384	-0.05032	0.010255
Cd-optB86	-0.82276	-0.23037	-0.53733
Co-optB86	-0.49326	-0.29379	-0.24942
Cr-optB86	-0.23236	-0.06932	-0.06189
Cu-optB86	-0.65632	-0.30982	-0.32594
Fe-optB86	-0.23178	-0.03296	0.020124
Hf-optB86	0.433302	0.299516	0.294822
Ir-optB86	-0.41192	-0.29665	-0.22835
Mn-optB86	0.058653	0.238191	0.275901
Mo-optB86	0.299466	0.141132	0.210159
Nb-optB86	0.246181	0.221493	0.243546
Ni-optB86	-0.15675	0.10024	0.120459
Os-optB86	-0.22969	-0.1232	-0.03839
Pd-optB86	0.042504	0.321464	0.270509
Pt-optB86	0.210886	0.30456	0.380071
Re-optB86	0.021504	0.112033	0.172515
Rh-optB86	-0.48424	-0.34218	-0.29412
Ru-optB86	-0.32885	-0.19562	-0.13137
Sc-optB86	-0.31512	-0.24923	-0.28912
Ta-optB86	0.339938	0.219313	0.262528
Ti-optB86	0.29605	0.29603	0.296
V-optB86	0.048249	0.197824	0.239768
W-optB86	0.139293	0.176189	0.247819
Y-optB86	-0.36712	-0.24725	-0.30596
Zn-optB86	-0.81048	-0.45232	-0.50729
Zr-optB86	0.430743	0.303139	0.291163
Ag-PBE	-0.77274	-0.41023	-0.41335
Au-PBE	-0.6414	-0.16759	-0.10585
Cd-PBE	-0.9103	-0.54991	-0.62939
Co-PBE	-0.56882	-0.39411	-0.34762
Cr-PBE	-0.33528	-0.18656	-0.18076
Cu-PBE	-0.75717	-0.43586	-0.45052
Fe-PBE	-0.27765	-0.10096	-0.04644
Hf-PBE	0.338389	0.205875	0.207196
Ir-PBE	-0.49331	-0.39189	-0.31533
Mn-PBE	0.005751	0.164986	0.202179

Mo-PBE	-0.03989	0.052373	0.128726
Nb-PBE	0.152278	0.140655	0.157559
Ni-PBE	-0.2872	-0.05002	-0.02727
Os-PBE	-0.3066	-0.2093	-0.11721
Pd-PBE	-0.06685	0.227788	0.146169
Pt-PBE	0.125179	0.210736	0.29249
Re-PBE	-0.05902	0.019547	0.086375
Rh-PBE	-0.70686	-0.58105	-0.52925
Ru-PBE	-0.39743	-0.28017	-0.21018
Sc-PBE	-0.41587	-0.35432	-0.38857
Ta-PBE	0.249634	0.128454	0.176582
Ti-PBE	0.20542	0.2054	0.20533
V-PBE	-0.03456	0.107845	0.148109
W-PBE	0.044242	0.086891	0.165599
Y-PBE	-0.46634	-0.35517	-0.39848
Zn-PBE	-0.89895	-0.43972	-0.60753
Zr-PBE	0.336672	0.209829	0.203926

Ti_2CO_2-STM electrical conductivity and thermodynamic stability.

The electrical conductivity is another important factor that affects the catalytic performance besides the catalytic activity. We know that Ti_2CO_2 is a semiconductor material. The band gap calculated by LDA + U method is 0.42 eV, which is satisfied to the reference value [1]. Corresponding to different U values, we calculated the energy band structures of Ti_2CO_2-STM with better HER catalytic activity than Ti_2CO_2. As shown in **Figure S1**, except Ti_2CO_2-Mn (E_{gap} = 0.475 eV), Ti_2CO_2-V, Nb, Mo, W and Re are all transformed from semiconductors to conductors, thus allowing high charge transfer kinetics during the HER.

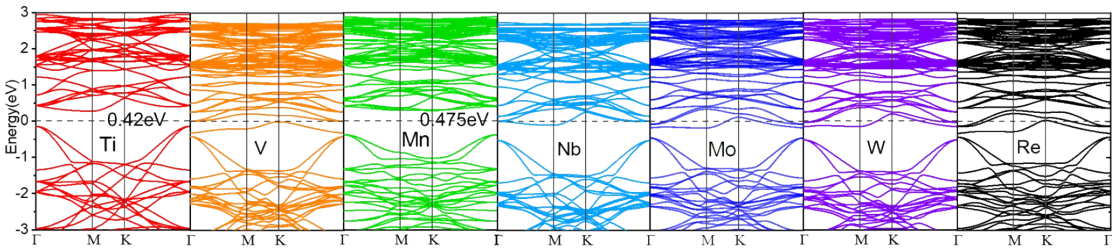

Figure S1. Band structure of Ti_2CO_2 and Ti_2CO_2-V, Mn, Nb, Mo, W and Re. The band gaps of Ti_2CO_2 and Ti_2CO_2-Mn and others Ti_2CO_2-STM are 0.42 eV, 0.475 eV and 0 eV, respectively. The Femi level is set to zero.

To ensure the stability of Ti_2CO_2-STM, we calculated STM doping formation energy of and the *Ab initio* molecular dynamics (AIMD) at different temperatures (300K and 500K). It can be seen from **Figure S2 (a)** that the doping formation energies are all negative, indicating that they are more stable relative defects. At the same time, there is an obvious corresponding relationship between the doping formation energy and the position of the periodic table of the metal. As shown in **Figure S2 (a)**, the doping energies of 3d, 4d and 5d metal atoms are the most stable when they are in the same group as Ti, such as Zr and Hf. And the stability of the doped system in the same period decreases with the site deviation from Ti. This phenomenon also exists in the STM adsorbed on the surface of 2D MXenes [1]. This trend is beneficial to select the STM for the experimental synthesis. The structures of Ti_2CO_2-STM with excellent catalytic activity and conductivity were found to be also relatively stable, and the stability order was Nb > V > Mo > W > Mn > Re.

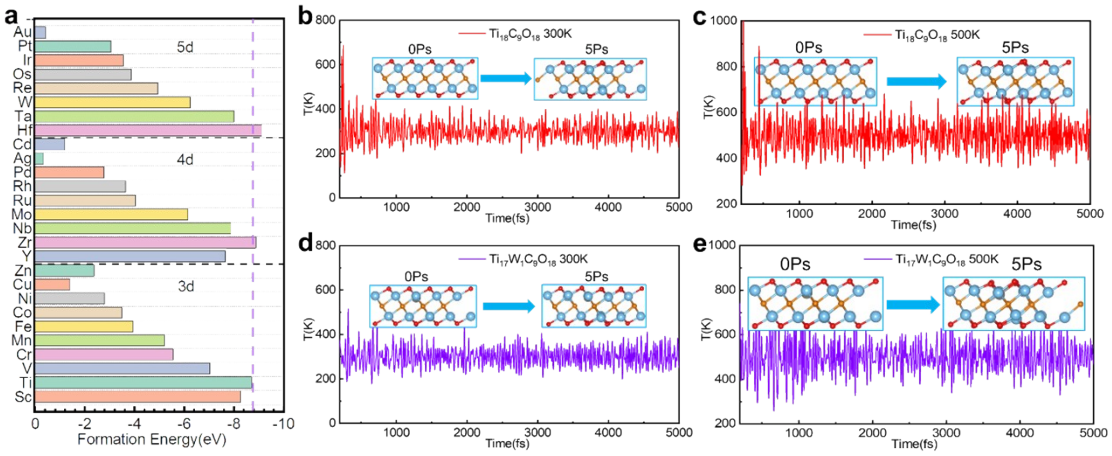

Figure S2. Thermodynamic stability. (a) The formation energies of 3d, 4d and 5d STM doping in Ti vacancy of Ti_2CO_2; (b, c) AIMD of Ti_2CO_2 at 300K and 500k; (d, e) AIMD of Ti_2CO_2-W at 300K and 500k.

In order to further verify the stability of Ti_2CO_2-STM, we studied the thermodynamic stability of Ti_2CO_2 and Ti_2CO_2-STM by AIMD under NVT ensemble. As shown in **Figure S2 (b)**, the overall morphology of Ti_2CO_2 or Ti_2CO_2-STM remains at 300K and 500K, even though the change is obvious at 500K than at 300K. Taking Ti_2CO_2-W with good catalytic activity, conductivity and metal doping defect stability as an example, it is found that the structure of Ti_2CO_2-W remains relatively stable at 300K and 500K.

According to the above analysis of catalytic activity, band structure and stability, it is found that the STM doping can effectively improve the catalytic performance of 2D Ti_2CO_2 for HER. Ti_2CO_2-W, Nb, V, Mo and Re show excellent catalytic activity, conductivity and structural stability of HER, among which Ti_2CO_2-W has outstanding performance.

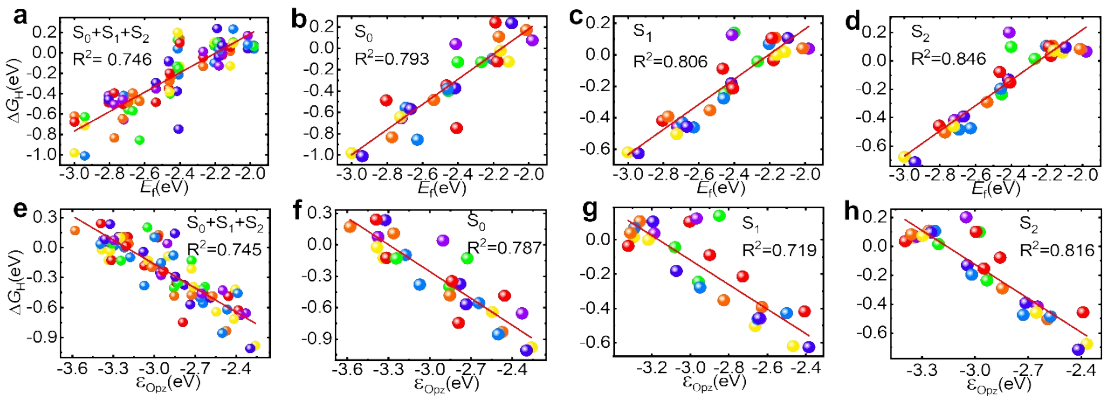

Figure S3. The correlation coefficients between Fermi level (E_f), P_z-band center of O (ε_{Opz}) and adsorption energy ΔG_H of S_0, S_1, S_2 sites.

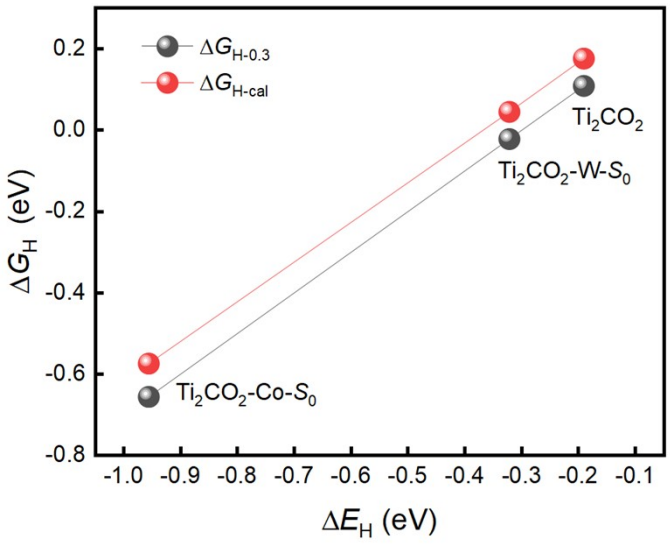

Figure S4. Comparison of methods to simplify ΔE_{ZPE} - TΔS_H.

In Eq. (6), 0.3 eV is applied to replace ΔE_{ZPE} - TΔS_H from ref.[2]. And from ref.[3], the ΔE_{ZPE} - TΔS_H of Ti_2CO_2 is replaced by 0.265eV.

To evaluate the impact of simplification in using 0.3 eV to replace ΔE_{ZPE} - TΔS_H, we re-calculate ΔG_H using the formula $\Delta G_H = \Delta E_H + \Delta E_{ZPE}$ - TΔS_H with 3 samples, as shown in **Figure S4**. The $\Delta G_{H-0.3}$ is the ΔG_H calculated by using 0.3eV to replace ΔE_{ZPE} - $T\Delta S_H$, and ΔG_{H-cal} is calculated using Eq. (4), which is shown in **Table S4**.

Table S4. 3 Samples for the calculation of ΔE_{ZPE} - TΔS_H.

Sample	$E_{ZEP}^{H^*}$	E_{ZPE}^*	$-\frac{1}{2}E_{ZEP}^{H_2}$	-TΔS_H	ΔE_{ZPE} - TΔS_H
Ti_2CO_2	0.2998	0	-0.135	0.202	0.367
Ti_2CO_2-W-S_0	0.3003	0	-0.135	0.202	0.367
Ti_2CO_2-Co-S_0	0.2981	0	-0.135	0.202	0.365

As shown in **Figure S4**, ΔE_{ZPE} - TΔS_H is about 0.367eV. Therefore, the difference between ΔG_{H-cal} and $\Delta G_{H-0.3}$ is one constant term equal to 0.067eV. The Ti_2CO_2-W-S_0 are still close to zero with $\Delta G_{H-0.3\,(Ti_2CO_2-W-S_0)} = -0.022$eV, $\Delta G_{H-cal\,(Ti_2CO_2-W-S_0)} = 0.045$eV. The absolute values are smaller than the absolute values of $\Delta G_{H-0.3\,(Ti_2CO_2)} = -0.109$eV and $\Delta G_{H-cal\,(Ti_2CO_2)} = -0.176$ eV separately. The simplification for ΔE_{ZPE} - TΔS_H used in this paper does not affect the filter result.

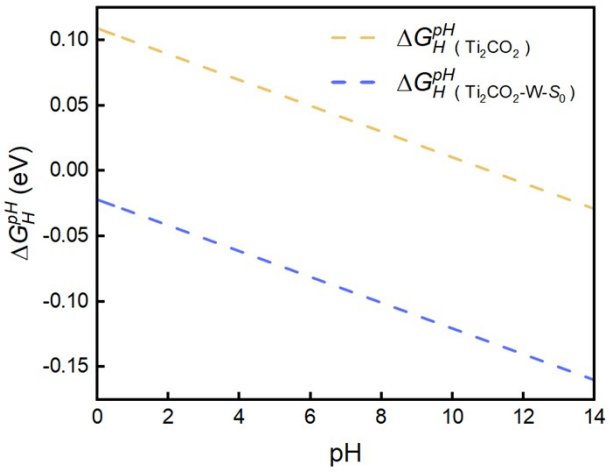

Figure S5. ΔG_H^{pH} vs pH.

The stability of Ti_2CO_2-W-S_0 under the standard hydrogen electrode and pH values is shown in **Figure S5**. The ΔG_H^{pH} is calculated by Eq. (9), and calculation details are added in Methods. As shown in **Figure S5**, with pH from 0 to 14, $|\Delta G_H^{pH}|$ is within 0.170 eV. The stability of Ti_2CO_2-W in different pH environments is acceptable.

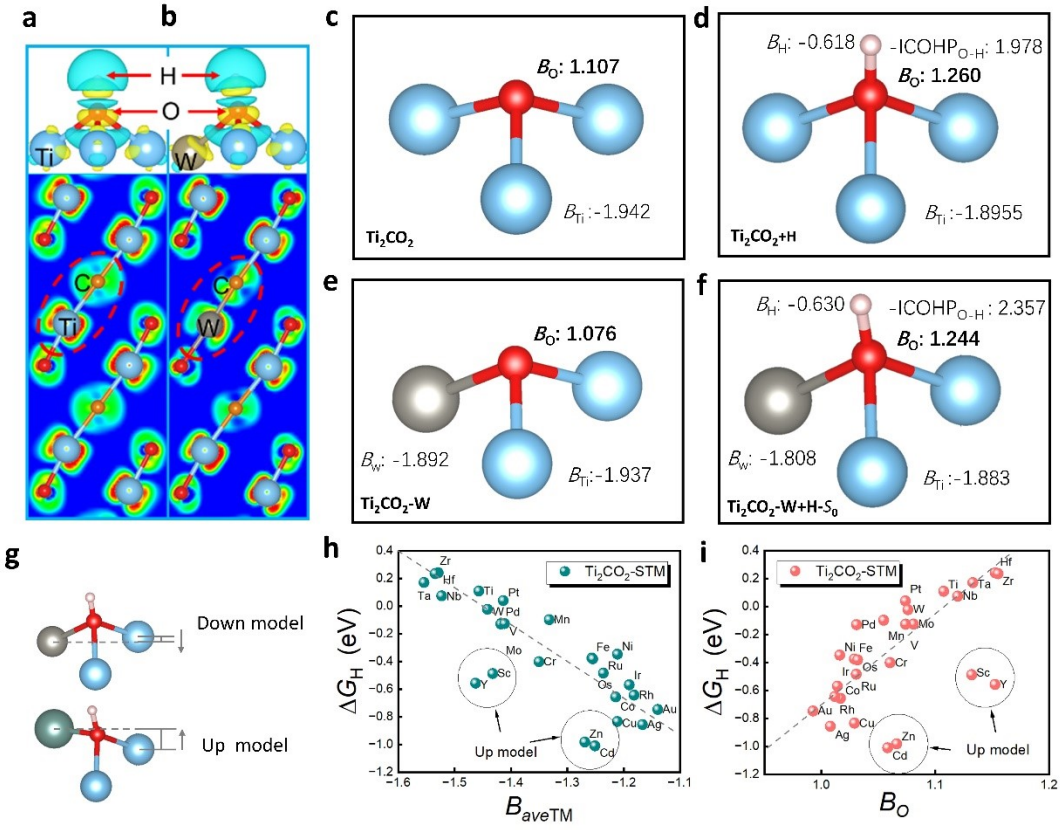

Figure S6. Deformation charge density and Bader analysis. (a) Deformation charge density for Ti_2CO_2+H and (b) Ti_2CO_2-W+H-S_0. (c-f) Bader charge for Ti_2CO_2, Ti_2CO_2-W+H, Ti_2CO_2-W, Ti_2CO_2-W+H-S_0, the positive Bader charge (B) means electron gain. (g) MXenes structure model. (h-i) ΔG_H vs the average Bader charge of 3 metal atoms below O atoms (B_{aveTM}), and ΔG_H vs the by Bader charge of O atom (B_O).

As shown in **Figure S6 (a)** and **(b)**, the electron interaction of Ti-C and W-C bonds differs significantly in both the charge distribution direction and intensity. The O-Ti/W-C-Ti-O interaction acts as a chain that changes the electronic configuration of Ti-C and W-C directly affecting the electronic structure of the surface O atom. From **Figure S6 (c)** and **(e)**, the electron transfer number for the O atom (Bo) from Ti and W for Ti_2CO_2-W is significant less than for Ti_2CO_2. Therefore, comparing Ti_2CO_2+H **(d)** and Ti_2CO_2-W+H-S_0 **(f)**, $B_{H\,(Ti_2CO_2+H)}$ =- 0.618e and $B_{H\,(Ti_2CO_2-W+H-S_0)}$ =- 0.630e. These show that the H atom in Ti_2CO_2-W+H-S_0 offers more electrons to match the ability of oxygen atoms to gain electrons, which leads to stronger bonding of O-H and lower adsorption energy.

We generalized the above conclusions to all Ti_2CO_2-STM systems. The **Figure S6 (h)** shows ΔG_H

affected by the average Bader charge of 3 metal atoms below O atoms (B_{aveTM}) for Ti_2CO_2-STM without H absorption. **Figure S6 (i)** shows the ΔG_H affected by the Bader charge of O atom (B_O) for Ti_2CO_2-STM without H absorption. For most doping systems, ΔG_H decreases with increase of B_{aveTM}, which shows that the ΔG_H mechanism for W has is generally good for most Ti_2CO_2-STM. In addition, the Sc, Y, Zn, Cd doping atoms, which have large atomic radii compared to the Ti atom, are located higher along the z axis than the Ti layer if doped in Ti_2CO_2 (**Table S5**). The structure model is shown in the Up model of **Figure S6 (g)**. When the doping atoms are located higher than Ti layer, even for the O layer along the z axis, the doping atoms and H are undergoing a direct interaction and electron transfer after H absorption at the S_0 site. The correlation between ΔG_H and B_{aveTM} or B_O for Sc, Y, Zn, Cd doping atoms in **(h)** and **(i)** is not shown. Therefore, alone Bader charge is inadequate to describe ΔG_H. Thus, the descriptor for ΔG_H need further exploration.

Table S5. Δh values between STM and Ti atom layer along the z axis.

Name	Δh (Å)	Name	Δh (Å)	Name	Δh (Å)
Ag	-0.0923	Mo	-0.2908	Ta	-0.0019
Au	-0.1253	Nb	-0.0309	Ti	0
Cd	0.3512	Ni	-0.2811	V	-0.3012
Co	-0.3531	Os	-0.3921	W	-0.2569
Cr	-0.2991	Pd	-0.1847	Y	0.54591
Cu	-0.2531	Pt	-0.1970	Zn	0.24214
Fe	-0.3765	Re	-0.3641	Zr	-0.0841
Hf	0.0925	Rh	-0.2920		
Ir	-0.3363	Ru	-0.3572		
Mn	-0.2656	Sc	0.22732		

Table S6. Comparation of ΔG_H and ΔG_H (H_2O).

Sample	E_*	E_* (H_2O)	E_{H*}	E_{H*} (H_2O)	ΔG_H	ΔG_H (H_2O)
Ti_2CO_2	-415.850	-415.912	-419.428	-419.790	0.109	-0.156
Ti_2CO_2-W-S_0	-418.493	-418.602	-422.202	-422.480	-0.023	-0.201
Ti_2CO_2-W-S_1	-418.493	-418.602	-422.202	-422.443	2.988 E-05	-0.173
Ti_2CO_2-W-S_2	-418.493	-418.602	-422.202	-422.371	0.073	-0.094

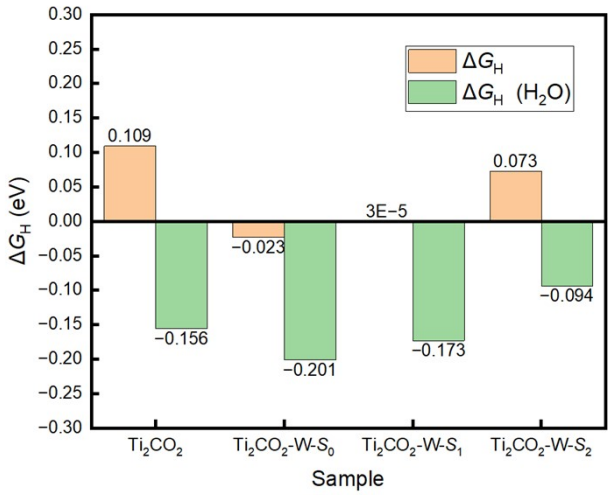

Figure S7. Effect of H_2O solvent.

The effect of H_2O solvent is calculated by the VASPsol [4] method. As shown in **Table S6**, the free energy E_* (H_2O) of about 0.10 eV decreases to E_* , but after H absorption, The free energy E_{H*} (H_2O) decreases by 0.25 eV compared to E_{H*}. The final ΔG_H with the H_2O solvent effect is shown in **Figure S7**. The result is in accord with the conclusion from ref.[5]. The O terminal is hardly affected by the solvent, whereas the H terminal is affected significantly.

In total, $|\Delta G_H (H_2O)|$ of Ti_2CO_2-W with H_2O solvent is in the range of 0.20 eV. It retains good catalytic capacity in the H_2O solvent.

Table S7. Descriptor subsets for GPR and SVR model.

Number	Descriptor-GPR	R^2 (3-fold CV) -GPR	Descriptor-SVR	R^2 (3-fold CV) -SVR
5	$[E_f, d_{M_1-O}, R_M, B_M, CH_M]$	0.931	$[E_f, d_{M_1-O}, R_M, B_M, \varepsilon_{Md}]$	0.922
4	$[E_f, d_{M_1-O}, R_M, \varepsilon_{Md},]$	0.928	$[E_f, d_{M_1-O}, B_M, \varepsilon_{Md},]$	0.921
3	$[E_f, d_{M_1-O}, R_M]$	0.901	$[E_f, d_{M_1-O}, \varepsilon_{Opz}]$	0.891
2	$[E_f, d_{M_1-O}]$	0.855	$[E_f, d_{M_1-O}]$	0.834
1	$[E_f]$	0.63	$[E_f]$	0.76

The combinations of descriptors giving the optimal results from GPR and SVR models, are shown in **Table S7**. The 2 key descriptors E_f and d_{M_1-O} are still the most import descriptors for both the GPR and SVR models. The importance of the atom radius of the dopant metal (R_M) is seen in the GPR model. R_M also shows the structural change due to the MXenes surface. This suggests that the HER for doping MXenes system is controlled by size factors as well.

Reference

1. Peng, Q., Zhou, J., Chen, J., Zhang, T. & Sun, Z. Cu single atoms on Ti2CO2 as a highly efficient oxygen reduction catalyst in a proton exchange membrane fuel cell. *J. Mater. Chem. A* **7**, 26062–26070 (2019).
2. Gao, G., O'Mullane, A. P. & Du, A. 2D MXenes: A New Family of Promising Catalysts for the Hydrogen Evolution Reaction. *ACS Catal.* **7**, 494–500 (2017).
3. Meng, Z. *et al.* MXenes modified by single transition metal atom for hydrogen evolution reaction catalysts. *Appl. Surf. Sci.* **562**, 150151 (2021).
4. Mathew, K., Sundararaman, R., Letchworth-Weaver, K., Arias, T. A. & Hennig, R. G. Implicit solvation model for density-functional study of nanocrystal surfaces and reaction pathways. *J. Chem. Phys.* **140**, (2014).
5. Xu, H., Cheng, D., Cao, D. & Zeng, X. C. A universal principle for a rational design of single-atom electrocatalysts. *Nat. Catal.* **1**, 339–348 (2018).